JOM, Vol. 72, No. 6, 2020
https://doi.org/10.1007/s11837-020-04047-1
© 2020 The Minerals, Metals & Materials Society

Microstructure and Fracture Toughness of Compact TiC-Fe Gradient Coating Fabricated on Cast Iron Substrate by Two-Step In Situ Reaction

HAIQIANG BAI,[1,2,3] LISHENG ZHONG,[1,3,4] ZHAO SHANG,[1,3] PENGJIE CUI,[1,3] LING KANG,[1,3] ZHENLIN LV,[1,3] and YUNHUA XU[1,2,3,5]

1.—School of Material Science and Engineering, Xi'an University of Technology, Xi'an 710048, People's Republic of China. 2.—School of Chemistry and Chemical Engineering, Yulin University, Yulin 719000, People's Republic of China. 3.—International Research Center for Composite and Intelligent Manufacturing Technology, Xi'an University of Technology, Xi'an 710048, People's Republic of China. 4.—e-mail: zhonglisheng1984@163.com. 5.—e-mail: xuyunhua@xaut.edu.cn

A compact TiC-Fe gradient coating with high hardness and toughness has been fabricated on cast iron by two-step in situ reaction. The phase constitution of the coating was TiC and α-Fe. As the thickness of the coating was increased, the size (about 6.34 μm to 0.54 μm) and volume fraction of TiC particles gradually decreased. The formation mechanism of TiC was nucleation-growth of TiC grains (the first step of the in situ reaction) and the diffusion-type solid-phase transition via diffusion of carbon atoms into the titanium lattice (the second step of the in situ reaction). From the surface of the coating to the coating–substrate interface, the hardness and elastic modulus gradually decreased from 30.74 ± 0.61 GPa and 438.47 ± 4.82 GPa to 21.67 ± 1.03 GPa and 380.71 ± 5.86 GPa, respectively. Meanwhile, the fracture toughness gradually increased from 3.21 MPa $m^{1/2}$ to 6.75 MPa $m^{1/2}$.

INTRODUCTION

In practical engineering applications, many components are usually subjected to severe working conditions such as high speed, high pressure, and heavy load. The surface of the part is subjected to strong wear and impact loads for a long time, resulting in failure. Transition-metal carbides are widely used as a protective coating on mechanical parts due to their high hardness, excellent wear resistance, and good corrosion resistance, greatly extending the service life of tools and machines.[1–3] Although the abrasion resistance of the surface of the component can be improved by increasing the hardness, this leads to a decrease in toughness. For engineering structural components, it is critical to have both high strength and high toughness, but unfortunately, strength and toughness are often conflicting properties characteristics.[4,5] To break this inverse relationship between strength and toughness, many strategies have thus been applied to improve the strength and toughness of the coating simultaneously. These mainly include constructing a gradient structure,[6] triggering phase-transformation toughening,[7] incorporating a high-toughness phase,[8] or forming a nanostructure composite coating.[9–11] Among these methods, the preparation of a gradient structure coating on the metal surface is considered to be one of the most effective ways to achieve enhanced hardness yet high toughness coatings.[6,12,13] Compared with traditional uniform ceramic coatings, gradient structured coatings offer unique advantages:[14–18] (1) a gradient variation of the microstructure from the surface of the coating to the substrate, reducing the stress in the internal structure of the coating, (2) improved fracture toughness of the coating, and (3) a gradient connection at the interface, which can significantly reduce the interface mismatch stress, thereby improving the interfacial bonding strength between the coating and substrate. To date, many surface modification techniques have been used to prepare such gradient coatings, including laser cladding (LC),[19,20] plasma spraying (PS)[21–23] and

(Published online February 10, 2020)

thermoreactive deposition and diffusion (TRD).[24,25] The LC technique uses a laser beam to simultaneously melt the coating material and the surface of the substrate with rapid solidification to form a surface coating. A gradient coating is then prepared by changing the proportion of the precoated powder and placing it on the surface of the coating prepared in the previous step and cladding. Shi et al.[19] used a LC method to prepare a gradient composite coating on 20CrMnTi low-carbon alloy steel substrate. The coating and substrate exhibited a good interfacial transition, and the wear resistance of the gradient composite coating was enhanced by 36.4-fold compared with the steel substrate. In the PS technique, a plasma arc is used to heat a precoated powder to a molten or semimolten state and spray it onto the surface of the workpiece at high speed to form a surface coating, during which a gradient coating can be prepared by changing the ratio of the powder. Rezapoor et al.[21] successfully prepared a TiC-Fe gradient coating on 45 steel substrate using PS technology. From the surface of the coating to the substrate, the volume fraction of TiC particles decreased from 100% to 25%, which significantly reduced the residual stress at the interface between the coating and substrate and improved the interfacial bonding strength. In TRD, the substrate material is immersed in a bath of molten borax containing associated strong carbide-forming elements such as vanadium, titanium, and niobium, which react with carbon atoms in the substrate; then, as the reaction proceeds, the nucleation density decreases and the grain size increases, thereby forming a gradient coating. Fan et al.[25] used the TRD technique to prepare a vanadium carbide gradient coating with a thickness of only 8 μm on AISI H13 steel substrate. Although these preparation techniques can be used to prepare gradient coatings, they still suffer from many disadvantages. For LC, the grains are prone to coarsening during solidification and the volume fraction of the carbide reinforcement is limited. With PS, the coating typically has a porous structure which reduces the hardness and wear resistance of the coating.[22] Meanwhile, TRD is only used for the preparation of thin coatings.[24,25] Therefore, it is necessary to develop new techniques for the preparation of gradient structure coatings owing to their interest for toughness, wear resistance, and extended applications.

In the work described herein, a compact TiC-Fe gradient coating with high hardness and toughness was successfully fabricated on cast iron by two-step in situ reaction. The microstructure exhibited a significant gradient in the grain size and volume fraction of TiC particles in the thickness direction of the coating. The coating–substrate interface presented a perfect metallurgical bond because of the in situ formation of TiC particles. Moreover, the TiC-Fe gradient coating achieved superhardness (30.74 GPa to 21.67 GPa) and excellent toughness (3.21 MPa $m^{1/2}$ to 6.75 MPa $m^{1/2}$) due to the gradient transformation of the microstructure and excellent interfacial bonding.

EXPERIMENTAL PROCEDURES

Preparation of TiC-Fe Gradient Coating

A rolled titanium (99.9%) plate was selected as the titanium source. Gray cast iron with chemical composition of Fe-3.21C-1.050Mn-1.320Si-0.077P-0.240Cr (in wt.%) was used as the substrate material. The procedure for the production of the specimen was as follows: First, the titanium plate (10 mm × 10 mm × 1 mm) and iron substrate (10 mm × 10 mm × 5 mm) were ground using SiC sandpaper and ultrasonically cleaned in absolute ethyl alcohol for 10 min. Second, the cast iron with the titanium plate on top was first heated up to 1160°C in a horizontal tube furnace at a heating rate of 5°C/min. Subsequently, it was immediately cooled to 1085°C with the furnace (the first step of the in situ reaction). The temperature was held for 2 h. Finally, the sample was immediately quenched in water (the second step of the in situ reaction).

Microstructural Characterization

To characterize the microstructure, the produced specimen was ground and polished. The phase constituents on the cross section and surface of the specimen were determined by x-ray diffraction (XRD) analysis (SmartLab 9 kW; Rigaku, Japan). The cross-sectional microstructure of the TiC-Fe gradient coating was examined by scanning electron microscopy (SEM; Zeiss, Germany) equipped with energy-dispersive spectroscopy (EDS) and electron backscattered diffraction analysis (EBSD; Nordlys-Nano, Oxfordshire, UK). EBSD data including a band contrast map, phase map, pole figure, and inverse pole figure were obtained using HKL Channel 5 software. In addition, the crystal structure and interface lattice correlation between different phases were investigated by field-emission transmission electron microscopy (TEM, JEM-3010).

Property Testing

The hardness (H) and elastic modulus (E) in the cross section of the coating were measured using a Nanoindenter G200 (Agilent, Oak Ridge, USA) with a test force of 450 mN. Based on the maximum indentation depth (h_{max}) and residual indentation depth (h_r) obtained from the load–displacement curve, the plastic deformation rate (Δp) of the coating was calculated using the following formula:[26]

$$\Delta p = (h_r/h_{max}) \times 100\%. \quad (1)$$

In addition, the indentation morphology, crack length, and half-diagonals of the indentation imprint were characterized by SEM. Based on the

values of the hardness, elastic modulus, crack length (l), and half-diagonals of the indentation imprint (a) obtained by the nanoindentation method, with respect to the Palmqvist crack configuration, the fracture toughness (K_{IC}) of the TiC-Fe gradient coating was evaluated using the following equation:[6,27,28]

$$K_{IC} = k\left(\frac{a}{l}\right)^{1/2}\left(\frac{E}{H}\right)^{2/3}\frac{P}{C^{3/2}}, \qquad (2)$$

where k is a constant (k = 0.016), P is the applied load (N), and C is the total length of a and l.

RESULTS AND DISCUSSION

Microstructure and Phase Composition

Figure 1a presents the XRD results obtained from the cross-section of the as-fabricated sample, revealing a phase composition of graphite (G), α-Fe, Ti, and TiC. Since the remaining titanium plate was not ground off before XRD analysis, the diffraction peak for metal Ti is observed in Fig. 1a. The appearance of G and α-Fe phases is attributed to the iron substrate, because it contains graphite flake and ferrite. To further understand the phase composition of the coating, the remaining titanium plate was ground off before the surface of the coating was analyzed by XRD. As illustrated in Fig. 1b, the XRD pattern of the surface of the carbide coating contained only TiC phase, indicating that the topmost surface of the coating was a layer of almost pure TiC. The XRD results for TiC are in good agreement with previously published reports.[27,29–32]

Figure 2a displays the representative cross-sectional microstructure of the as-fabricated sample. A newly generated TiC-Fe layer with thickness of approximately 31.8 ± 0.46 μm is clearly observed between the titanium plate and iron substrate. The interface between the TiC coating and the substrate exhibits good metallurgical bonding, with no cracks or voids observed. Additionally, it is apparent that a significant microcrack is present between the layer cross section and the remaining titanium plate. This is caused by the concentration of residual stress at the interface. Since the thermal expansion coefficients of the pure Ti (10.2×10^{-6}/K) and TiC phase

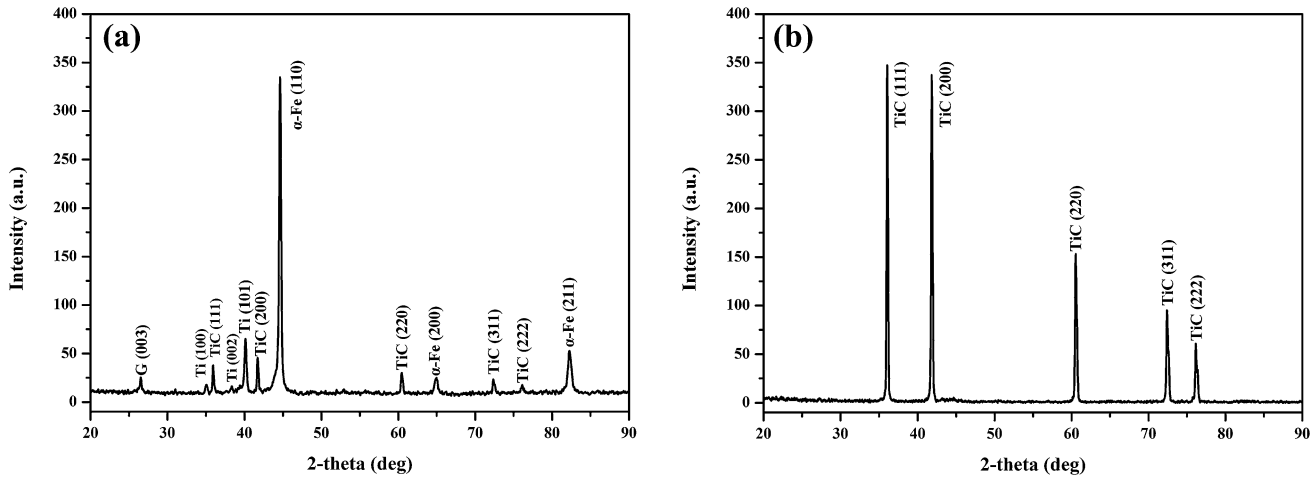

Fig. 1. (a) Cross-section XRD pattern of specimen and (b) surface XRD pattern of carbide coating.

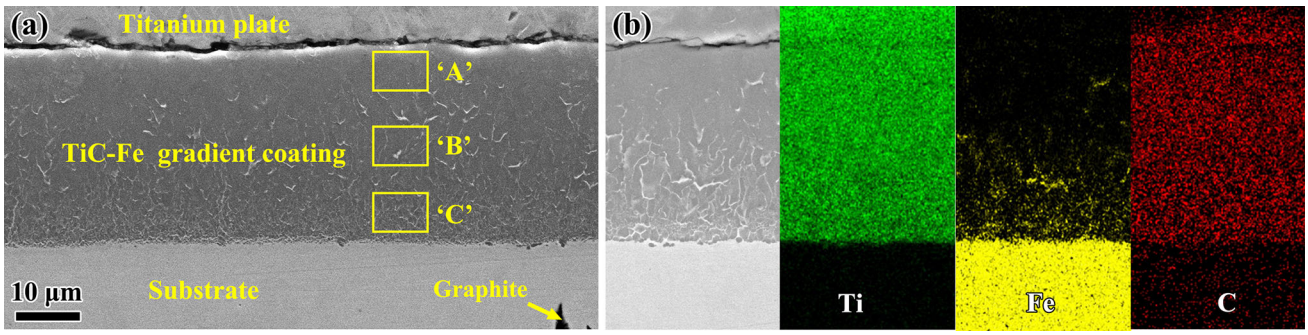

Fig. 2. (a) SEM morphology and (b) EDS element distribution maps for the cross section of the as-fabricated sample.

(7.74×10^{-6}/K) are very different, when the sample is quenched in water after heat treatment, a large tensile stress is generated at the interface between the titanium plate and the TiC layer, which causes interface cracking between the titanium and the coating. For this reason, the remaining titanium plate on the surface of the coating is easily peeled off, which indicates that the process is ideal for the preparation of iron-based surface coatings. Furthermore, to achieve a good understanding of the chemical composition of the coating, EDS analysis was carried out on the cross section of the as-fabricated sample. Figure 2b presents the EDS element mapping images of the coating, revealing that the white phase in the coating (Fig. 2) is α-Fe phase. The EDS results are in good agreement with the XRD results in Fig. 1a. Moreover, the α-Fe phase exhibits a gradient distribution from the interface of the Ti/TiC-Fe coating to the TiC-Fe coating/substrate interface. Thus, the TiC-Fe gradient coating can be successfully prepared on the surface of the iron substrate.

To further investigate the phase distribution, the morphology of the TiC particles, and the orientation of the TiC and α-Fe phases, EBSD characterization was carried out on the cross section of the TiC-Fe gradient coating (Fig. 3). In Fig. 3a, the TiC grains are equiaxed, and the grain size decreases gradually from about 6.34 μm to 0.54 μm with depth, forming a gradient microstructure. Figure 3b reveals that the TiC-Fe gradient coating consisted of a harder TiC phase with a small amount of α-Fe phase, consistent with the XRD (Fig. 1) and EDS results (Fig. 2b). The volume fraction of TiC phase in the coating was estimated to be approximately 86% by EBSD. Figure 3c displays the growth orientation of the TiC particles in the coating, while the specific growth direction of the TiC particles can be determined based on the inverse pole figure. In addition, the growth orientation of the crystal can also be represented by pole figures, which show the orientation of a family of crystal faces in space on a spatial stereo projection, as shown in Fig. 3d and e. This result reveals that the crystal orientations of

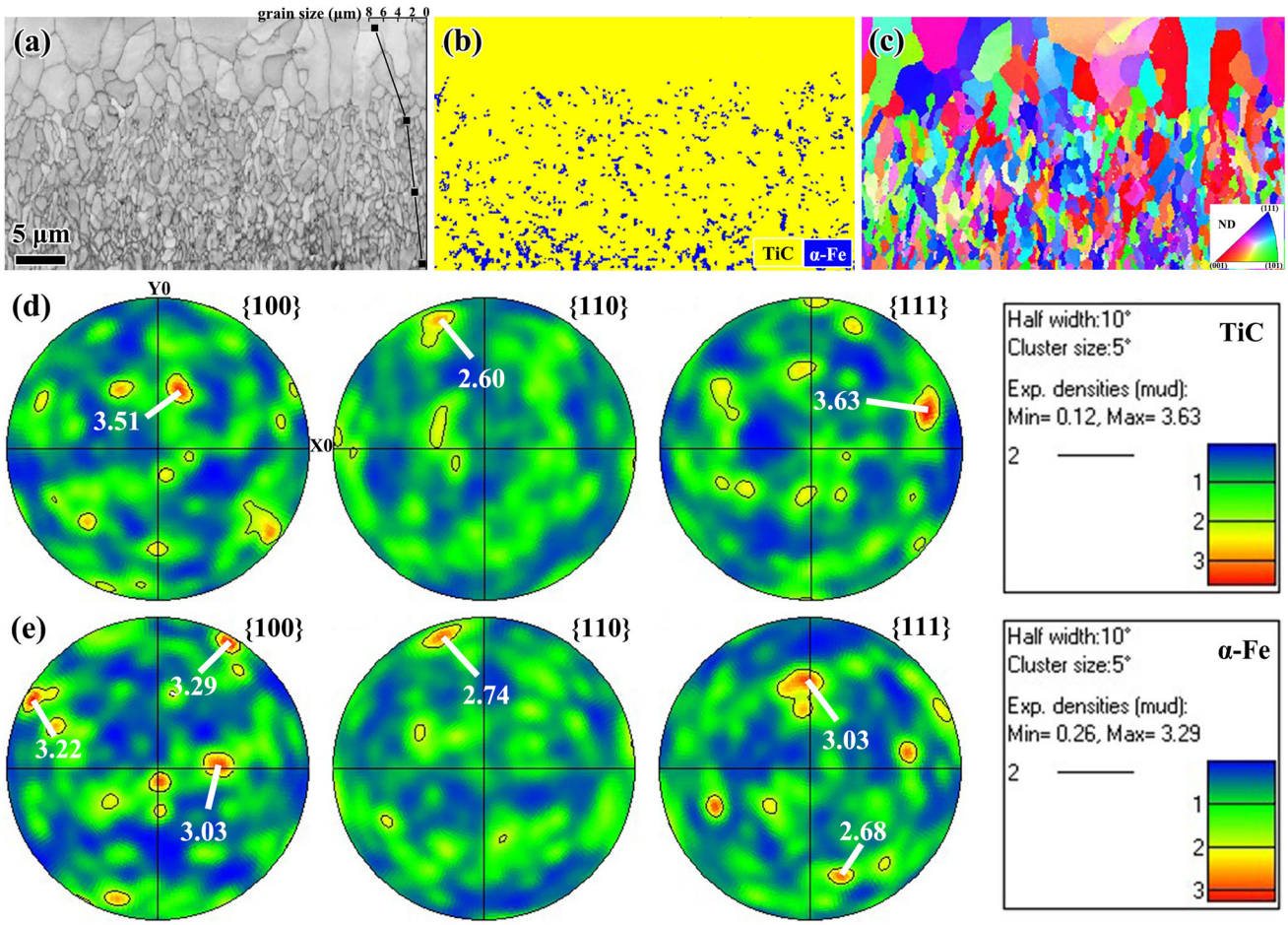

Fig. 3. EBSD patterns on cross section of TiC-Fe gradient coating: (a) band contrast map, (b) spatial distribution of TiC and α-Fe phase, (c) crystallographic orientation map and inverse pole figure; and pole figures of (d) TiC and (e) α-Fe phase. The curve of grain size as a function of depth is inserted in (a).

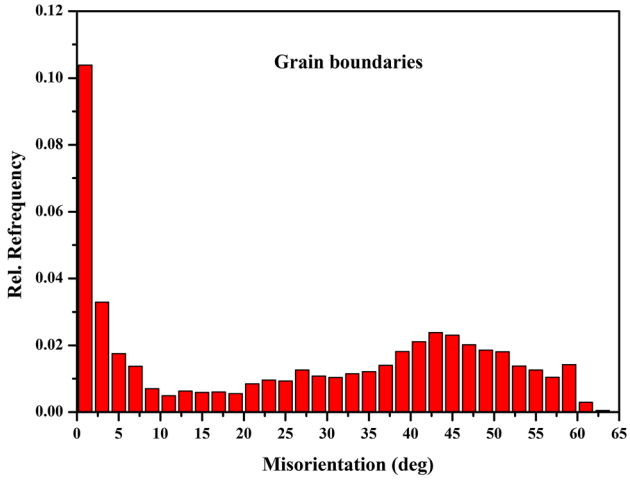

Fig. 4. Misorientation distribution for TiC particles.

the TiC and α-Fe phases in the TiC-Fe gradient coating were randomly distributed. The grain boundaries can be described by the misorientation angle. Figure 4 displays the misorientation angle distributions of the grain boundaries of TiC particles obtained from the cross section of the coating shown in Fig. 3a. The misorientation between the TiC grains is mainly distributed in the range from 0° to 65°, with a clear high preference for orientation angles between 0° and 2.5°, indicating that the grain boundaries between TiC particles are mainly small-angle grain boundaries (< 10°).

To further identify the phase composition and lattice structure in the TiC-Fe gradient coating, TEM measurements were performed at different positions on the cross section of the coating (Fig. 2a). Figure 5a represents bright-field TEM images taken at position "A" in Fig. 2a. The corresponding selected-area electron diffraction (SAED) pattern is indexed as the diffraction pattern of face-centered cubic (fcc) TiC along the [011] zone axis (Fig. 5b). Figure 5c presents a HRTEM image taken between two adjacent TiC particles (Fig. 5a) with interplanar spacing of 0.2473 nm and 0.2516 nm, respectively, which can be indexed as the (111) lattice plane of TiC. Moreover, note that the TiC grain boundary is metallurgically bonded and semi-coherent. Figure 5d presents a bright-field TEM image taken at position "B" in Fig. 2a. Based on the SAED and HRTEM images (Fig. 5e and f), it can be identified that the α-Fe phase is distributed along the grain boundaries of the TiC particles. This indicates that no other phase (Fe_2Ti and FeTi) is formed during the in situ reaction, consistent with the XRD and EBSD results. The corresponding lattice interface relationship between the TiC and α-Fe phases is a semicoherent interface. Figure 5g shows a bright-field TEM image taken at the TiC-Fe coating/substrate interface. The corresponding SAED pattern identifies the two constituent phases as body-centered cubic (bcc) α-Fe and fcc TiC. Thus, the phase composition of the TiC-Fe gradient coating is mainly TiC phase with α-Fe phase distributed along the grain boundaries of the TiC particles. Moreover, the microstructure exhibits a significant gradient in the grain size and volume fraction of TiC particles in the thickness direction of the coating, consistent with the SEM (Fig. 2a) and EBSD (Fig. 3a) results.

Based on the above analysis of the microstructure, it is evident that the TiC-Fe coating presented the structural characteristic of a gradient distribution of particle size and volume fraction of TiC. A similar structure has been reported in previous studies[6,19,21] and can reduce the thermal mismatch stress concentration at the interface between the coating and substrate. Moreover, the gradient variation of the coating can significantly improve the bonding strength of the interface between the coating and substrate as well as the fracture toughness of the coating.

Formation Mechanism of TiC-Fe Gradient Coating

In this study, the TiC-Fe gradient coating was fabricated on cast iron by two-step in situ reaction (1160°C + 1085°C × 2 h). The microstructure was completely dense, consisting of TiC particles (∼ 86%) and α-Fe phase. The morphology, size, and volume fraction of the TiC particles presented a gradient change with increasing coating thickness. The formation of the TiC-Fe gradient coating can be illustrated as follows: During the first step of the in situ reaction, when the temperature is less than 1148°C, carbon atoms hardly diffuse due to the simple mechanical contact between the cast iron and titanium plate. When the temperature lies between 1148°C and 1160°C, the cast iron melts to form a Fe-C molten pool, and the titanium atoms desolventize from the titanium plate into the molten pool, thereby forming a Ti-Fe-C ternary system molten pool between cast iron and titanium. Based on thermodynamic calculations,[27,33] Ti has a large negative energy of formation (− 166.17 kJ/mol, 1160°C) with C than that of Fe element in the melt pool. Therefore, [Ti] and [C] have a great driving force to form [TiC], namely [Ti] + [C] = [TiC]. During the cooling process (1160°C to 1080°C), [TiC] rapidly precipitates, nucleates, and grows from the melt, while at the same time, α-Fe is distributed along the grain boundaries of the TiC particles to form a thin TiC-Fe layer. During this process, the formation mechanism of TiC is nucleation–growth of TiC grains. The purpose of the first step of the in situ reaction is to form a good metallurgical bond at the interface of the titanium and iron, to promote the interfacial transport of carbon atoms. In the second step of the in situ reaction, since both the cast iron and titanium are solid, the formation of the TiC-Fe layer is controlled by the diffusion of carbon atoms. This is because the radius of the carbon atom (R_C = 0.91 Å) is smaller than that of the titanium

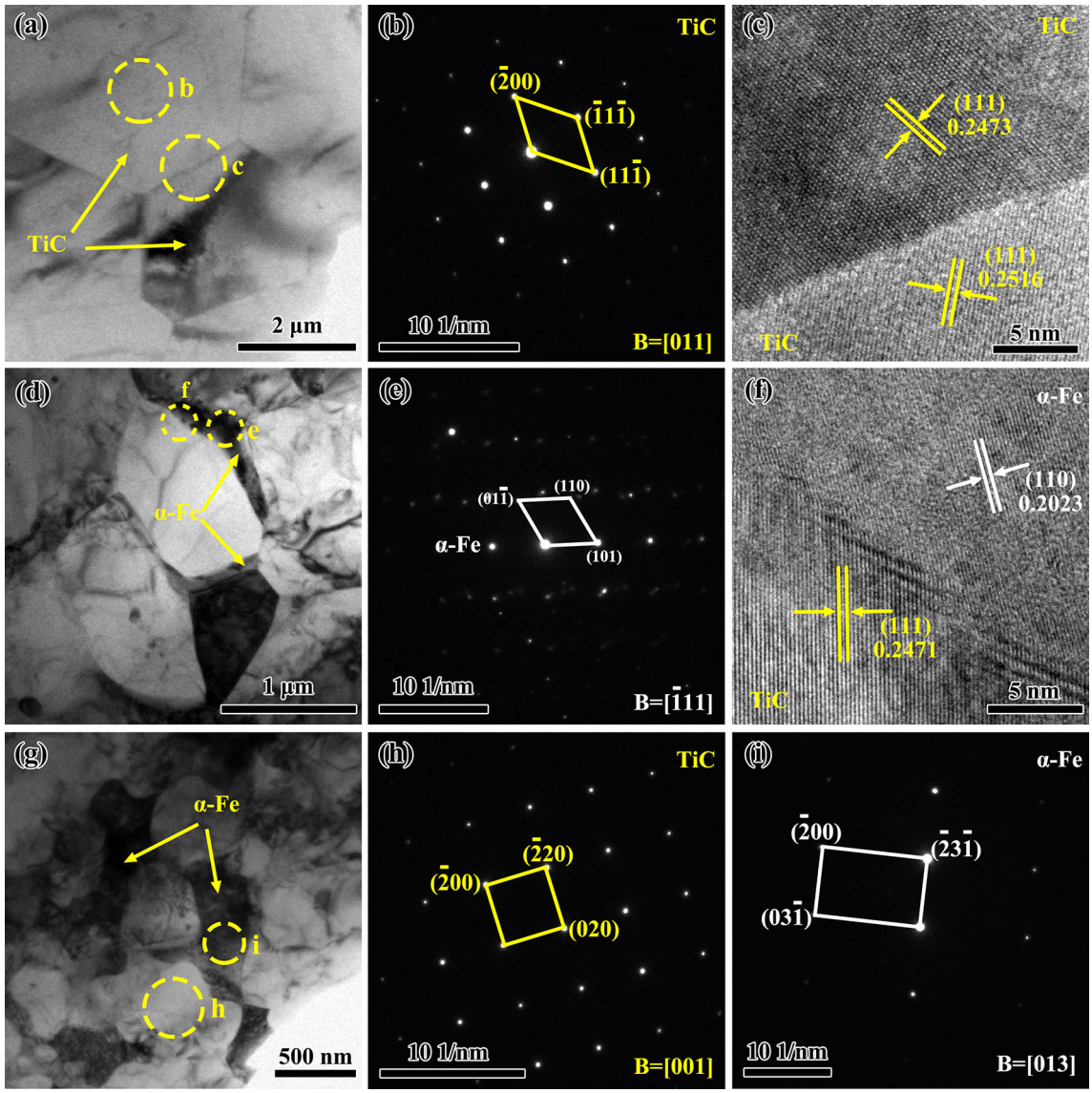

Fig. 5. TEM images of TiC-Fe gradient coating: (a) bright-field TEM image taken at position "A" in Fig. 2(a); (b, c) corresponding SAED pattern of TiC particle and HRTEM pattern of TiC/TiC interface as indicated in (a); (d) bright-field TEM images taken at position "B" in Fig. 2(a); (e, f) corresponding SAED pattern of α-Fe phase and HRTEM pattern of α-Fe/TiC interface as indicated in (d); (g) bright-field TEM images taken at position "C" in Fig. 2(a); (h, i) corresponding SAED patterns of TiC and α-Fe phase as indicated in (g).

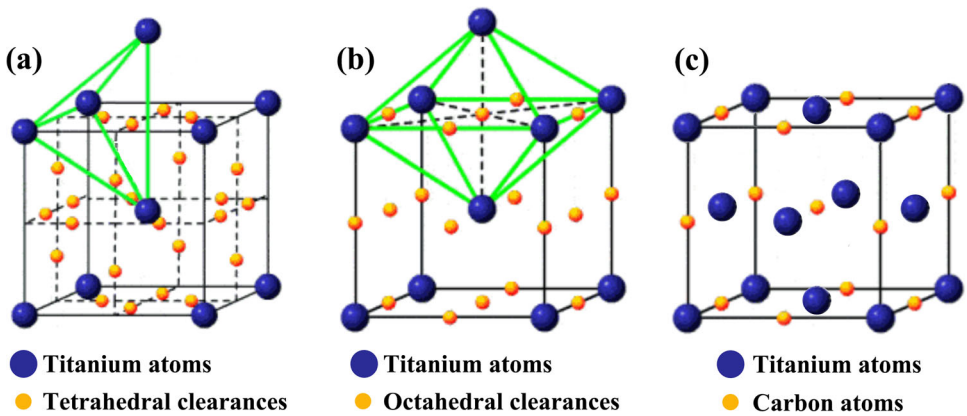

Fig. 6. (a) Tetrahedral and (b) octahedral clearances in the unit cell of bcc β-Ti. (c) Unit cell of fcc TiC.

atom (R_{Ti} = 2.0 Å), so the diffusion rate of carbon atoms in the TiC-Fe layer is greater than that of titanium atoms.[34] The ratio of the radius of the C atom to the Ti atom is

$$\frac{R_C}{R_{Ti}} = \frac{0.91}{2.0} = 0.455. \quad (3)$$

As shown in Fig. 6a and b, the radius of the tetrahedral and octahedral clearances along the <100> direction in the crystal lattice of bcc β-Ti is $0.291R_{\beta\text{-Ti}}$ and $0.154R_{\beta\text{-Ti}}$, respectively, being insufficient to hold a carbon atom. However, the radius of the octahedral clearances along the <110> direction in the crystal lattice of bcc β-Ti is $0.633R_{\beta\text{-Ti}}$, which is sufficient to hold a carbon atom. Due to effective strain relief, carbon atoms preferentially occupy octahedral vacancies.[27] Therefore, carbon atoms diffuse into the titanium lattice to form face-centered cubic (fcc)-structured TiC via a diffusion-type solid-phase transition (Fig. 6c), whose reaction can be expressed as Ti + C = TiC. At the same time, Fe atoms are distributed at the TiC grain boundaries by diffusion. As the reaction progresses, the thickness of the TiC-Fe layer increases continuously, resulting in a decrease in the diffusion rate of carbon atoms and Fe atoms. Therefore, the nucleation density of TiC gradually decreases, while the grain size of TiC particles gradually increases. Furthermore, Zhang et al.[31] found that the size of the TiC particles increased with decreasing iron content, which may be because the α-Fe phase inhibits grain growth by preventing grain boundary migration during heat conduction, resulting in grain refinement.[35] Thus, the sizes of the TiC particles are mainly determined by the nucleation density (carbon concentration) and the α-Fe content. The formation mechanism of the TiC particles is the diffusion-type solid-phase transition via the diffusion of carbon atoms into the titanium lattice (the second step of the in situ reaction). The formation mechanism of the TiC-Fe gradient coating is the change of the TiC nucleation density caused by the carbon concentration gradient.

Compared with previous work,[29,30] relatively fine TiC particles could be obtained here because the microstructure was "frozen" and the movement of the grain boundaries was suppressed.[36] In addition, due to the difference in thermal expansion coefficient between titanium and TiC, interface cracking between the titanium and TiC-Fe layer was obtained by controlling the cooling method, while the coating and substrate still represent a good combination. Subsequently, the remaining titanium plate was easily peeled off using pliers. Local adhesion of titanium to the surface of the coating usually occurred but could be removed by simple mechanical polishing. Therefore, this process is an ideal method for preparing iron-based surface gradient coatings.

Mechanical Properties and Toughening Mechanism of TiC-Fe Gradient Coating

In a coating/substrate system, the strength and toughness of the coating are important parameters that determine its service environment and ability to withstand the impact load. Therefore, the nanoindentation method was used to evaluate the H, E, K_{IC}, and deformation behavior of the TiC-Fe gradient coating. Figure 7a presents the distribution of H and E as a function of coating thickness. From the surface of the coating to the coating/substrate interface, the values of E and H gradually decreased from 30.74 ± 0.61 GPa and 438.47 ± 4.82 GPa to 21.67 ± 1.03 GPa and 380.71 ± 5.86 GPa, respectively. Generally, the hardness of TiC_x varies with the Ti/C stoichiometry.[37,38] However, in this work, due to the high carbon content in the cast iron (3.21 wt.%), there was sufficient carbon to react with titanium to form TiC by in situ reaction. Hence, the gradual decrease in H and E is primarily dependent on the gradient variation of the size and volume fraction of the TiC particles in the TiC-Fe coating. The H and E values obtained for the surface of the coating were approximately eight times those of the iron substrate (3.54 GPa and 163.56 GPa, respectively). Thus, the TiC-Fe gradient coating significantly improved the hardness of the surface of the iron substrate. Figure 7b displays the corresponding load–displacement curve. Pop-in is seen during the loading process, indicating that the coating cracked under the action of the load.[39] In addition, based on the maximum indentation depth (h_{max}) and residual indentation depth (h_r) obtained from the load–displacement curve, the plastic deformation rate of the TiC-Fe gradient coating can be evaluated (Eq. 1). For indentation 1, indentation 2, and indentation 3, the degree of plastic deformation of the TiC-Fe gradient coating was approximately 63.97%, 66.71%, and 70.62%, respectively. Compared with the iron substrate (88.75%), the elastic deformation of the TiC-Fe gradient coating was improved, but it still exhibited better plastic deformation. This is because the coating contained a small amount of high-toughness α-Fe phase.

Figure 8 presents the corresponding nanoindentation imprint at different positions on the cross section of the TiC-Fe gradient coating. It can be observed that the cracks only originate at the corners of the indentation parallel to the coating, with no cracks appearing at the corners of the indentation at 90° to the coating. Moreover, the crack at the corners of the indentation parallel to the coating does not propagate in the direction of the corners of the indentation but rather parallel to the direction of the coating. A similar phenomenon is observed in TaC-reinforced iron-based surface composites.[40] This may be because the coating exhibits a gradient variation in the thickness direction, while the layers are uniform in the direction parallel to the coating surface. Moreover, the TiC-Fe

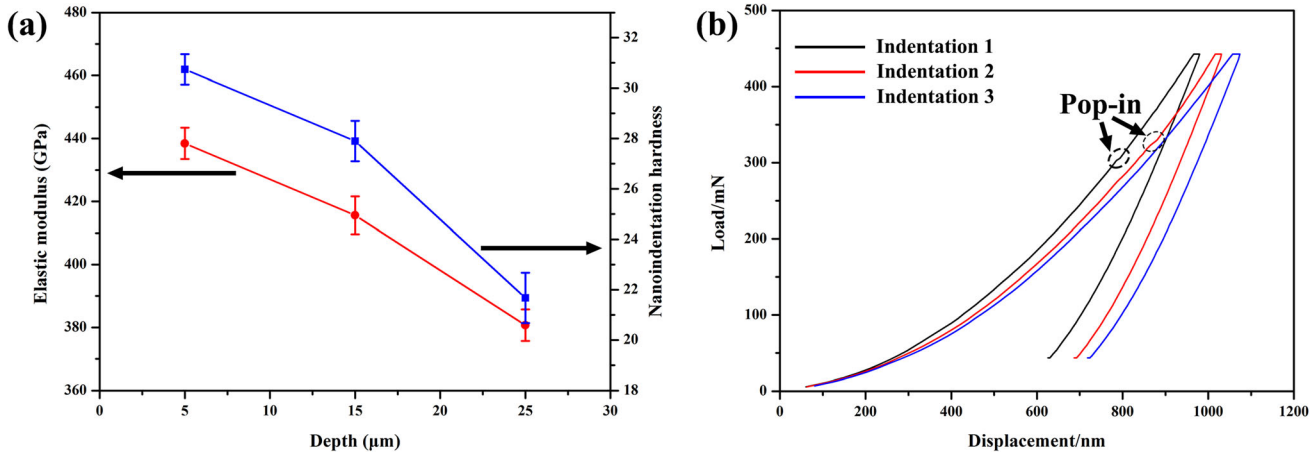

Fig. 7. (a) Nanoindentation hardness and elastic modulus distributions and (b) corresponding load–displacement curves of TiC-Fe gradient coating along the depth direction.

gradient coating has a certain layered orientation, and there is a certain anisotropy macroscopically, which will cause the coating to resist anisotropic crack propagation. Therefore, the crack propagation resistance in the direction parallel to the surface of the coating is weaker than that in the direction vertical to the coating, so it is easier to initiate cracks parallel to the coating surface under load. The crack length (L) and the half-diagonals of the indentation imprint (a) were measured using SMile-View software. Using the values of H, E, L, and a in Eq. 2, for indentation 1, indentation 2, and indentation 3, the K_{IC} values of the TiC-Fe gradient coating were determined to be 3.21 ± 0.38 MPa $m^{1/2}$, 4.02 ± 0.46 MPa $m^{1/2}$, and 6.75 ± 0.53 MPa $m^{1/2}$, respectively. These results suggest that the toughness was significantly dependent on the microstructure and phase composition of the TiC-Fe gradient coating. The gradual decrease in the toughness value is related to the gradient distribution of TiC particles (grain size and volume fraction) and α-Fe phase in the coating.

To further understand the toughening mechanism of the TiC-Fe gradient coating, the crack propagation path in the indentation morphology was analyzed. As shown in Fig. 8a, radial and circumferential cracks were observed at the corners of the indentation and the indentation edges, respectively. Moreover, crack deflection was also seen during radial crack propagation. When the coating is subjected to the load, the material around the indenter undergoes a sharp deformation, forming a large strain stress field.[41] To release energy, some areas of stress concentration initiate radial cracks. To maintain the driving force for crack propagation, the crack tends to be weak interface cracking (grain boundary/phase boundary).[42] Based on the EBSD and TEM characterization (Figs. 3 and 5c), the TiC particles showed no significant growth orientation in the coating. Therefore, when the crack tip encounters a TiC/TiC grain boundary, it will propagate along the grain boundary due to the interface mismatch; namely, the crack will be deflected. Such crack deflection causes an increase in the total crack propagation path, thereby reducing the driving force for crack propagation. The circumferential cracks form around the indentation because the size of the TiC particles is approximately 5 μm to 6 μm while the size of the indentation is only about 5 μm, so the indenter is almost inside the TiC particles rather than at the grain boundaries, thus creating a larger circumferential compressive stress around the indenter. In addition, when the crack tip encounters the tough α-Fe phase, the tough phase is deformed so that the stress field at the crack tip is relaxed, the crack is passivated, and the crack propagation is suppressed (Fig. 8b and c). When the plastic dissipation of the ductile phase is insufficient to offset the crack tip extension driving force, crack bridging with the α-Fe phase as the bridging phase is easily formed.[27,41] Therefore, in addition to its own toughness contribution, the α-Fe phase can also achieve the purpose of toughening by changing the crack propagation path.

In summary, this TiC-Fe gradient coating prepared by an in situ reaction method achieved comprehensive mechanical properties in terms of hardness, elastic modulus, and toughness in comparison with other hard ceramic coatings.[3,6,13,18,43] The improvement of the mechanical properties is mainly attributed to the high volume fraction of hard TiC phase particles (about 86%), the small amount of the high-toughness α-Fe phase, and the gradient variation of the microstructure, which may increase the load-carrying capacity of the TiC-Fe gradient coating.

CONCLUSION

A compact TiC-Fe gradient coating with high hardness and fracture toughness was successfully fabricated on cast iron by two-step in situ reaction (1160°C + 1085°C × 2 h). The TiC-Fe gradient

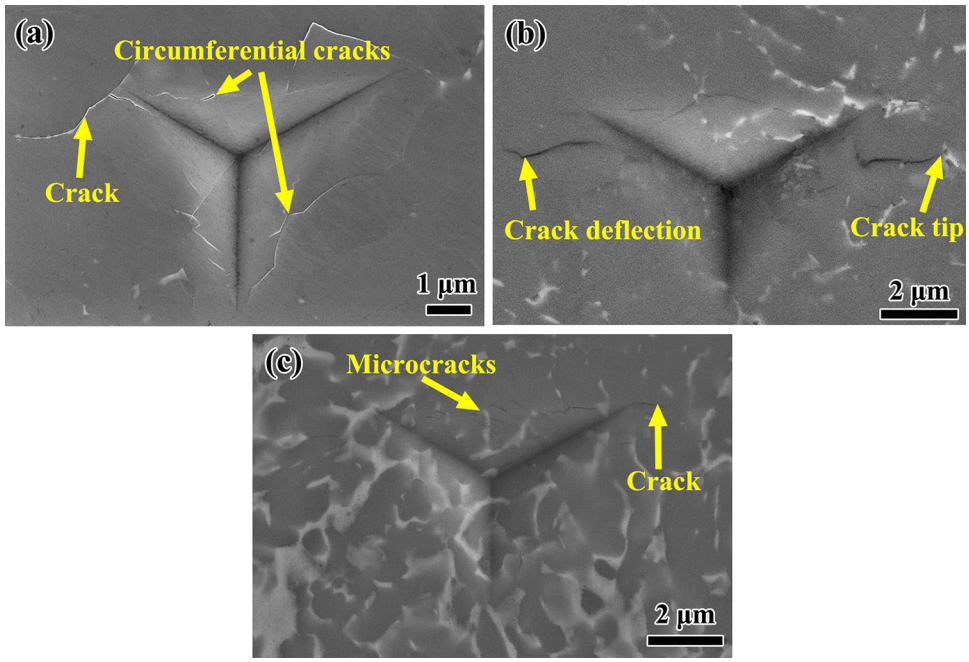

Fig. 8. Nanoindentation impression morphology at different zones on the cross section of the TiC-Fe gradient coating: (a) indentation 1, (b) indentation 2, and (c) indentation 3.

coating comprised TiC and α-Fe phases. The coating showed a gradient structure: from the surface of the coating to the substrate, the size of the TiC particles gradually reduced from about 6.34 μm to 0. 54 μm while the volume fraction of TiC gradually decreased. The formation mechanism of TiC particles is the nucleation–growth of TiC grains (the first step of the in situ reaction) and the diffusion-type solid-phase transition via diffusion of carbon atoms into the titanium lattice (the second step of the in situ reaction). The formation mechanism of the TiC-Fe gradient coating is the change of TiC nucleation density caused by the carbon concentration gradient. From the surface of the coating to the coating/substrate interface, the values of the hardness and elastic modulus gradually decreased from 30.74 ± 0.61 GPa and 438.47 ± 4.82 GPa to 21.67 ± 1.03 GPa and 380.71 ± 5.86 GPa, respectively. However, the value of the fracture toughness of the TiC-Fe gradient coating gradually increased from 3.21 MPa $m^{1/2}$ to 6.75 MPa $m^{1/2}$. This high hardness can mainly be attributed to the second-phase strengthening effect of the high volume fraction of the hard TiC phase hindering the dislocation motion under the applied load. The high toughness is mainly attributed to the gradient transformation of the microstructure and the crack passivation, crack deflection, and crack bridging caused by the high-toughness α-Fe phase, which reduces the crack propagation driving force.

ACKNOWLEDGEMENTS

The authors gratefully acknowledge the National Natural Science Foundation of China (Grant No. 51704232), Key-point Research and Invention Program of Shaanxi Province (Grant No. 2017ZDXM-GY-032), International Research Center for Composite and Intelligent Manufacturing Technology (Grant No. 2018GHJD-17), and Innovation Capability Support Program of Shaanxi Province (Grant No. 2019-TD019).

REFERENCES

1. J. Xiong, Z. Guo, M. Yang, W. Wan, and G. Dong, *Ceram. Int.* 39, 337 (2013).
2. M. Zhang, X. Liu, H. Shang, and J. Lin, *Surf. Coat. Technol.* 362, 381 (2019).
3. Q. Wang, F. Zhou, Q. Ma, M. Callisti, T. Polcar, and J. Yan, *Appl. Surf. Sci.* 443, 635 (2018).
4. R.O. Ritchie, *Nat. Mater.* 10, 817 (2011).
5. F. Bouville, E. Maire, S. Meille, B. Van de Moortele, A.J. Stevenson, and S. Deville, *Nat. Mater.* 13, 508 (2014).
6. X. Cai, Y. Xu, M. Liu, L. Zhong, and F. Bai, *J. Alloys Compd.* 712, 204 (2017).
7. K. Yalamanchili, I.C. Schramm, E. Jiménez-Piqué, L. Rogström, F. Mücklich, M. Odén, and N. Ghafoor, *Acta Mater.* 89, 22 (2015).
8. H. Ju and J. Xu, *Appl. Surf. Sci.* 355, 878 (2015).
9. S. Gupta, R. Sachan, A. Bhaumik, and J. Narayan, *Nanotechnology* 29, 45LT02 (2018).
10. J. Narayan, S. Gupta, A. Bhaumik, R. Sachan, F. Cellini, and E. Riedo, *MRS Commun.* 8, 428 (2018).
11. S. Gupta, R. Sachan, A. Bhaumik, P. Pant, and J. Narayan, *MRS Commun.* 8, 533 (2018).
12. N. Zhao, Y. Xu, X. Huang, L. Zhong, and J. Lu, *Ceram. Int.* 42, 18507 (2016).
13. H. Cetinel, B. Uyulgan, C. Tekmen, I. Ozdemir, and E. Celik, *Surf. Coat. Technol.* 174, 1089 (2003).
14. X. Jin, L. Wu, Y. Sun, and L. Guo, *Mater. Sci. Eng., A* 509, 63 (2009).
15. Y. Li, W. Zhang, J. Fei, D. Zhang, and W. Chen, *Mater. Sci. Eng. A* 391, 124 (2005).
16. M. Naebe and K. Shirvanimoghaddam, *Appl. Mater. Today* 5, 223 (2016).

17. N. Zhao, Y. Xu, L. Zhong, Y. Yan, K. Song, L. Shen, and V.E. Ovcharenko, *Ceram. Int.* 41, 12950 (2015).
18. M. Riabkina-Fishman, E. Rabkin, P. Levin, N. Frage, M.P. Dariel, A. Weisheit, R. Galun, and B.L. Mordike, *Mater. Sci. Eng. A* 302, 106 (2001).
19. M. Rezapoor, M. Razavi, M. Zakeri, M.R. Rahimipour, and L. Nikzad, *Ceram. Int.* 44, 22378 (2018).
20. Y. Shi, Y. Li, J. Liu, and Z. Yuan, *Opt. Laser Technol.* 99, 256 (2018).
21. D. Chen, D. Liu, Y. Liu, H. Wang, and Z. Huang, *Surf. Coat. Technol.* 239, 28 (2014).
22. A.S. Demirkıran and E. Avcı, *Surf. Coat. Technol.* 116, 292 (1999).
23. X. He, P. Song, X. Yu, C. Li, T. Huang, Y. Zhou, Q. Li, K. Lü, J. Lü, and J. Lu, *Ceram. Int.* 44, 20798 (2018).
24. M. Biesuz and V.M. Sglavo, *Surf. Coat. Technol.* 286, 319 (2016).
25. X. Fan, Z. Yang, C. Zhang, Y. Zhang, and H. Che, *Surf. Coat. Technol.* 205, 641 (2010).
26. Y. Ma, Y. Zhang, X. Yao, X. Zhang, X. Shu, and B. Tang, *Surf. Coat. Technol.* 226, 75 (2013).
27. H. Bai, L. Zhong, Z. Shang, Y. Xu, H. Wu, J. Bai, and Y. Ding, *J. Alloys Compd.* 771, 406 (2019).
28. D. Casellas, J. Caro, S. Molas, J.M. Prado, and I. Valls, *Acta Mater.* 55, 4277 (2007).
29. S. Fan, L. Zhong, Y. Xu, Y. Fu, and L. Wang, *Adv. Eng. Mater.* 17, 1562–1567 (2015).
30. L. Zhong, T. Wu, X. Zhang, S. Fan, L. Wang, and S. Chen, *Mater. Sci.* 21, 1392 (2015).
31. M. Zhang, Q. Hu, B. Huang, J. Li, and J. Li, *Int. J. Refract. Met. Hard Mater.* 29, 356 (2011).
32. J. Zhu, L. Zhong, Y. Xu, X. Cai, F. Bai, Y. Ding, Z. Lu, and H. Wu, *Vacuum* 155, 631 (2018).
33. H. Zhu, K. Dong, H. Wang, J. Huang, J. Li, and Z. Xie, *Powder Technol.* 246, 456 (2013).
34. A. Miriyev, M. Sinder, and N. Frage, *Acta Mater.* 75, 348 (2014).
35. X. Cai, L. Zhong, Y. Xu, Z. Lu, J. Li, J. Zhu, Y. Ding, and H. Yan, *J. Alloys Compd.* 747, 8 (2018).
36. I.W. Chen and X.H. Wang, *Nature* 404, 168 (2000).
37. S. Gupta, A. Moatti, A. Bhaumik, R. Sachan, and J. Narayan, *Acta Mater.* 166, 221 (2019).
38. J.A. Nicholas, W.G. Robin, and J.M. Ken, *J. Mater. Sci.* 42, 1884 (2007).
39. Z. Xie, M. Lugovy, N. Orlovskaya, T. Graule, J. Kuebler, M. Mueller, H. Gao, M. Radovic, and D.A. Cullen, *J. Alloys Compd.* 634, 168 (2015).
40. N. Zhao, Y. Zhao, X. Wang, K. Tang, Y. Xu, Y. Wei, F. Yan, W. Meng, L. Wu, and Y. Fei, *Mater. Res. Express* 5, 065 (2018).
41. R.O. Ritchie, *Mater. Sci. Eng. A* 103, 15 (1988).
42. A.G. Evans, *J. Am. Ceram. Soc.* 73, 187 (1990).
43. X. Cai, L. Zhong, Y. Xu, X. Li, and M. Liu, *Surf. Coat. Technol.* 357, 784 (2019).

Publisher's Note Springer Nature remains neutral with regard to jurisdictional claims in published maps and institutional affiliations.